

Ultrafast dynamics of photocurrents in surface states of 3D topological insulators

Jens Güdde and Ulrich Höfer

*Fachbereich Physik und Zentrum für Materialwissenschaften,
Philipps-Universität Marburg, D-35032 Marburg, Germany*

This article reviews experimental work on the ultrafast electron dynamics in the topological surface state (TSS) of three-dimensional (3D) topological insulators (TIs) observed with time- and angle-resolved two-photon photoemission (2PPE). The focus is laid on the generation of ultrafast photocurrents and the time-resolved observation of their decay. 2PPE not only allow to unambiguously relate the photocurrents to the spin-polarized electronic surface states. Probing of the asymmetric momentum distribution of the electrons carrying the current makes it possible to study the microscopic scattering processes that governs the unusual electron transport in the time domain. Ultrashort mid-infrared pump pulses permit not only a direct optical excitation of the TSS in Sb_2Te_3 but also lead to a strong asymmetry of the TSS population in momentum space. Two-dimensional band mapping of the TSS shows that this asymmetry is in fact representative for a macroscopic photocurrent while the helicity-dependence of the photocurrent is found to be small. The time-resolved observation of the photocurrent decay reveals a huge mean free path of the electrons in the TSS.

INTRODUCTION

Basic properties of three-dimensional topological insulators

Three-dimensional topological insulators have attracted a lot of attention because they are characterized by an insulating bulk and a conducting surface state with remarkable properties which are interrelated and induced by strong spin-orbit coupling in combination with time-reversal symmetry [1–4]. One of these properties is its topological protection which guaranties the existence of the topological surface state as long as time-reversal symmetry is not broken. This makes the TSS robust against nonmagnetic perturbations which is beneficial for application in real devices. Moreover, the TSS promises unique electron transport properties due its linear Dirac-like energy-momentum dispersion in combination with spin-momentum locking which results in a chiral spin structure in momentum space. On the one hand, this implies that electrical currents in the TSS are automatically spin-polarized because opposite linear momenta are linked to opposite spin orientations [5]. On the other hand, the linear dispersion results in a small phase space for inelastic electron-electron scattering of excited electrons as in graphene [6] while the chiral spin structure additionally suppresses momentum scattering with complete absence of direct backscattering [7]. This means that spin-polarized electric currents in the TSS are expected to flow ballistically over large distances which makes these surface states promising for use in ultrafast low-loss electronics and spintronics.

The verification and application of these unique transport properties, however, turned out to be rather difficult because this requires that the transport is in fact dominated by the TSS. This needs TIs with a sufficiently large bulk band gap and a TSS that covers this gap. Beside the first predicted 3D TI $\text{Bi}_{1-x}\text{Sb}_x$ [8], tetradymites such

as the binary chalcogenides Bi_2Se_3 , Bi_2Te_3 , and Sb_2Te_3 belong to the same class of three-dimensional topological insulators and are characterized by a single Dirac cone around $\bar{\Gamma}$ and a relatively large indirect band gap [2, 3] compared to other known 3D topological insulators. The largest band gap is found in Bi_2Se_3 but amounts to only about 300 meV. This makes these materials in fact to narrow-gap semiconductors and their transport properties depend sensitively on the actual position of the Fermi level E_F which is often governed by unintentionally doping. For this reason, transport measurements on TIs are commonly dominated by their bulk rather than their unusual surface properties. Bi_2Se_3 , for example, is found to be highly n-doped due to Se vacancies [9, 10] and its transport properties are dominated by the bulk conduction band. On the other hand, the corresponding shift of the energy of the Dirac point E_D below the Fermi energy E_F makes the topological surface state of Bi_2Se_3 accessible by angle-resolved photoelectron spectroscopy (ARPES). This made ARPES to the most important tool for the characterization of TIs and made it not only possible to verify the linear dispersion of the TSS very shortly after its prediction [2, 11, 12] but also to proof its chiral spin texture by combination of ARPES with spin-resolved detection [5].

Mechanisms for photocurrent generation

The generation of a photocurrent, in particular by using ultrashort laser pulses, opens the possibility to investigate the unusual transport properties of TIs in the time domain and on the time scale of the scattering processes that governs the charge transport. Several mechanisms and techniques for the optical generation of dc electrical currents in condensed matter are known which are particularly well established for the generation of photocurrents in the conduction band of bulk direct-band-gap semicon-

ductors. This includes a scheme that additionally allows for a coherent control of the size and direction of the photocurrent by tuning the relative phase of two phase-locked laser fields with photon energies $\hbar\omega$ and $\hbar\omega/2$, which simultaneously drive a one- and two-photon transition, respectively. This method has been at first used to induce electric [13–15] and spin currents [16, 17] in bulk direct-band-gap semiconductors and has been combined with time- and angle-resolved 2PPE to investigate the ultrafast dynamics of electric currents in image-potential states at a Cu(001) surface [18]. Recently, it has been demonstrated for epitaxially thin films of Bi_2Se_3 using photon energies that exceed the bulk band gap [19, 20]. The generation of a dc current by this process can be understood as third-order nonlinear optical rectification which allows to generate photocurrents even in unbiased centrosymmetric materials [21]. An exclusive current generation in a TSS by this method [22], however, requires phase-stable two-color coherent control at very low photon energies because of the small band gap of typical topological insulators.

Other methods for photocurrent generation are based on single-color excitation schemes such as the photogalvanic effect [23–25]. The PGE is a second-order nonlinear effect and is therefore forbidden in inversion symmetric systems such as the bulk of the tetradymites B_2Se_3 , Bi_2Te_3 and Sb_2Te_3 which share the same rhombohedral crystal structure with the space group D_{3d}^5 [26]. This makes it possible to generate photogalvanic currents in these materials by a single-color excitation exclusively at the surface where the inversion symmetry is broken. The helical spin structure of the TSS of three-dimensional TIs motivates to utilize the circular photogalvanic effect to generate a directional helicity-dependent photocurrent because the coupling of circular polarized light depends on the spin orientation of the surface electrons with respect to the photon momentum. For surfaces with rotation symmetry, such as the threefold symmetry of the (111) surface of the tetradymite TIs, the circular photogalvanic effect vanishes at normal incidence even if the spin orientation has an out-of-plane component [27] because the latter results in a threefold symmetric excitation which does not generate a net directional current [28]. At oblique incidence, however, a helicity-dependent photogalvanic current can be generated perpendicular to the plane of incidence [28–30]. A photogalvanic current can be also generated by linear polarized light, which is described by the linear photogalvanic effect. At the threefold symmetric (111) surface of the tetradymite TIs, the direction of a photocurrent generated by the linear photogalvanic effect depends on the orientation of the light polarization with respect to the mirror plane of the surface. In contrast to the circular photogalvanic effect, it is expected that the linear photogalvanic effect has its maximum magnitude at normal incidence [31]. For small frequencies that cannot induce interband transitions, the

linear photogalvanic effect is microscopically described by asymmetric scattering of the excited electrons that are accelerated by the oscillating electric field [31].

Junck *et al.* have theoretically studied the possibility to generate photocurrents through the photogalvanic effect by optical transitions between the occupied and unoccupied part of an isolated TSS and found that pure orbital coupling can neither generate a helicity-dependent nor a helicity-independent photocurrent [32]. Only if they include the very small Zeeman coupling between the spins of the electrons and the magnetic field of the light, they can predict a helicity-dependent photocurrent that is, however, very small because it scales with the square of the Zeeman coupling.

A competing process that is even allowed in the bulk of centrosymmetric media is the photon drag effect which describes photocurrent generation by momentum transfer from light to carriers [24, 25, 33]. It is not straightforward to distinguish the photogalvanic effect and the photon drag effect in experiments, because both processes share the same dependence on the light polarization. In contrast to the photogalvanic effect, however, a photocurrent induced by the photon drag effect changes its sign when the direction of light propagation is reversed. An unambiguous identification of surface photocurrents in the tetradymite TIs without a surface specific probe therefore requires the comparison of data taken under front and back side illumination [31, 34].

Two-photon photoemission (2PPE)

In contrast to conventional ARPES, which is restricted to the spectroscopy of occupied electronic states, two-photon photoemission (2PPE) can additionally access initially unoccupied states by populating them first with a short excitation pulse and photoemitting the excited electrons with a second pulse [35, 36]. This makes it not only possible to investigate the unoccupied TSS of intrinsically p-doped samples. By introducing a variable time-delay between these two pulses, 2PPE can be combined with ultrafast pump-probe spectroscopy [35, 37]. It has been also early combined with angle-resolved detection [35, 38, 39] and is then nowadays often called time-resolved ARPES (trARPES). This term, however, might suggest that the photoemission step only subsequently images the transiently excited population while the 2PPE process also includes coherent effects of the two-photon transition [40–42].

Time- and angle-resolved 2PPE is even capable to investigate electron transport on an ultrafast time scale if the initial optical excitation by the pump pulses creates an asymmetry in the momentum distribution of the electrons parallel to the surface, i.e. a photocurrent [18]. The time-resolved observation of the redistribution and decay of the initially inhomogeneous momentum distri-

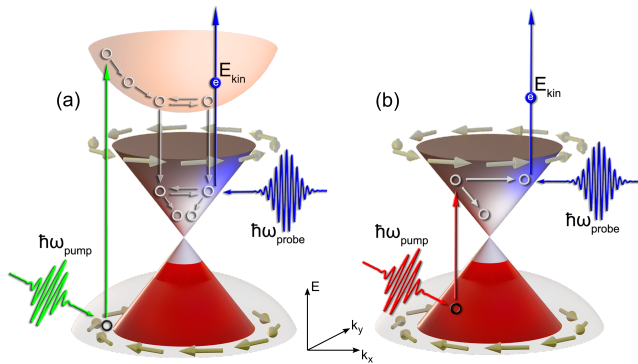


FIG. 1. Scheme for 2PPE of a partial filled TSS which is characterized by a Dirac-cone-like energy dispersion in the two-dimensional momentum space (k_x, k_y) of the surface and a chiral spin structure as indicated by the circulating arrows. (a) Pump pulses with photon energies that exceed the bulk band gap initially excite electrons in electronic bands far above the TSS under participation of many scattering events that homogenize the momentum distribution in the TSS even if the initial excitation might have induced an asymmetry in momentum space, i.e. a photocurrent. (b) Direct optical excitation of the unoccupied part of the TSS with mid-IR pump pulses. The subsequent photoemission images the initially generated momentum distribution and monitors its redistribution and decay on an ultrafast time scale.

tion provides microscopic information on the different scattering mechanisms of just those electrons that carry the photocurrent.

In the following, we will first review 2PPE experiments of TIs that utilize visible or near-infrared light for excitation. In section , we will then show that excitation of Sb_2Te_3 by linear polarized mid-infrared (mid-IR) pulses generates an inhomogeneous population of the TSS in momentum space (section) that can be unambiguously identified as a persistent macroscopic photocurrent by angle-resolved 2PPE covering both momentum directions of the surface band structure (section). This photocurrent is most pronounced if the excitation breaks the threefold symmetry of the $\text{Sb}_2\text{Te}_3(0001)$ surface, i.e. if the plane of oblique light incidence is aligned perpendicular to a mirror plane of the surface and vanishes for the opposite orientation. In spite of the helical spin texture of the TSS, the helicity dependence of the photocurrent is found to be small but can control the magnitude and sign of the photocurrent for the latter sample orientation (section). Decomposing the decay dynamics of the photocurrent into inelastic electron scattering to lower energies and elastic momentum scattering within the TSS reveals that the ballistic mean free path of the Dirac fermions reaches almost $1 \mu\text{m}$ resulting from the suppression of backscattering in the TSS (section). A similar large mean free path is found in Bi_2Te_3 by a novel combina-

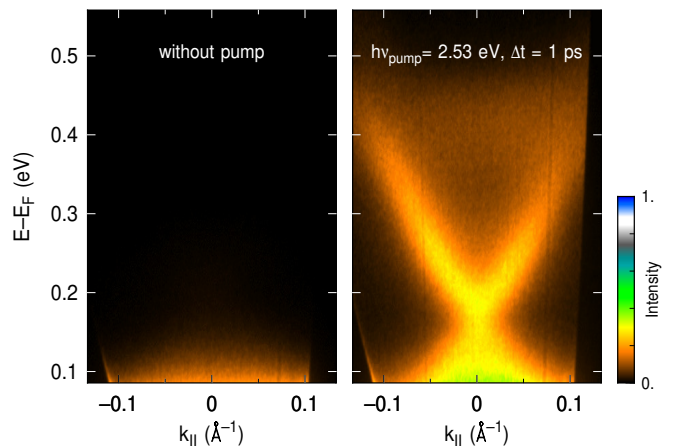


FIG. 2. Angle-resolved 2PPE spectra of Sb_2Te_3 . The electrons were collected along the $\bar{\Gamma}$ - \bar{K} direction, perpendicular to the plane of light incidence. A probe photon energy of 5.06 eV suppresses photoemission of the initially occupied states below E_F and enhances the dynamic range of the 2PPE signal. (a) without pump pulses. (b) 1 ps after arrival of the 2.53-eV pump pulses.

tion of THz acceleration of the Dirac fermions and time-resolved ARPES, which makes it possible to investigate electron transport just at the Fermi level with subcycle time resolution as is reviewed in section . These results present an unambiguous experimental verification of the unusual transport properties of the TSS of 3D topological insulators resulting from spin-momentum locking.

VISIBLE AND NEAR-IR EXCITATION

Most 2PPE studies on the TSS of TIs used pump pulses in the near-infrared or visible region [43–62]. Their photon energy therefore substantially exceeds the bulk band gap of the TIs. This typically prohibits a direct optical excitation of the TSS because the pump pulses predominantly excite electronic states with energies far above the TSS. Depending on the excitation conditions, this can include transitions for all combinations of bulk and surface initial and final states. These higher lying states decay subsequently to lower lying states which results in a delayed filling of the TSS [46, 53] as is depicted in Fig. 1(a). This typically prevents the generation of an asymmetry in the momentum distribution of the TSS and therewith a spin polarized photocurrent. Even if the initial excitation might induce such asymmetry in higher lying states [62], the sequential decay into the TSS close to the Fermi level goes along with multiple scattering events that homogenizes the momentum distribution.

While first 2PPE studies on TIs were investigating Bi_2Se_3 [43, 44, 46, 48–50] or Bi_2Te_3 [45, 52], the work presented here is focused on the third prototype 3D TI Sb_2Te_3 . Sb_2Te_3 is intrinsically p-doped, which is at-

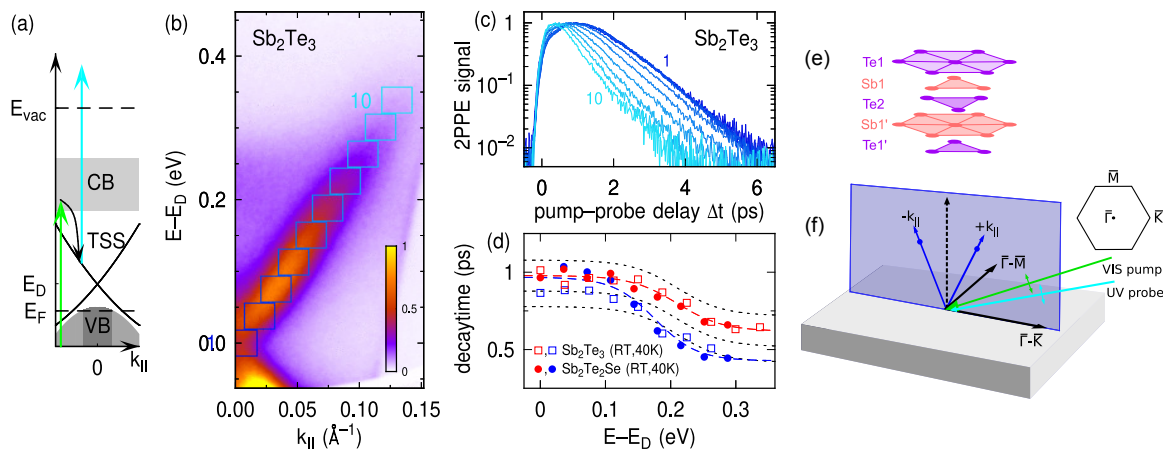


FIG. 3. (a) Excitation scheme for the population of the TSS with visible pump pulses via transfer from the bulk conduction band and subsequent photoemission with ultraviolet probe pulses. (b) 2PPE spectrum of the TSS of Sb_2Te_3 along the $\bar{\Gamma}-\bar{K}$ direction. The rectangles indicate the integration windows for the transient 2PPE intensities. (c) Transient 2PPE intensities of Sb_2Te_3 at room temperature (RT) within the integration windows shown in (b). (d) Decay times of the transient 2PPE intensities for Sb_2Te_3 (open squares) and $\text{Sb}_2\text{Te}_2\text{Se}$ (filled dots) at RT (red) and 40 K (blue), respectively. The dashed lines are guides to the eye. The black dotted lines indicate the variation of the decay times for different cleaves. Adapted with permission.[53] Copyright 2014, American Physical Society. (e) Structure of a quintuple layer of Sb_2Te_3 according to Ref. [3]. (f) Experimental geometry with sample orientation and surface Brillouin zone. In these experiments, the electrons were collected along the plane of light incidence.

tributed to substitutional Sb defects at Te sites [63], and most of the TSS is unoccupied. This makes it difficult to investigate the TSS by conventional ARPES [64, 65] and the Dirac-cone-like electronic structure of this prototype TI could until then only be verified indirectly by Landau level spectroscopy [66]. However, it makes Sb_2Te_3 an ideal system to study the electron dynamics within a TSS by 2PPE. The first 2PPE experiments on Sb_2Te_3 of Reimann *et al.* [53] have for the first time directly revealed that the massless Dirac-cone like energy dispersion of TSSs is in fact also realized in Sb_2Te_3 above the Fermi level as shown in Fig. 2.

This work furthermore compared the electronic structure and electron dynamics of Sb_2Te_3 with $\text{Sb}_2\text{Te}_2\text{Se}$ because theoretical predictions have suggested that the substitution of the central Te layer in the quintuple layers of Sb_2Te_3 (Te2 in Fig. 3(e)) by Se or S preserves the topological surface state, but considerably increases the bulk band gap [67, 68]. This should result in a better decoupling of the TSS from the bulk bands and therefore improve the transport properties. The 2PPE data on the dispersion of the TSS in both Sb_2Te_3 and $\text{Sb}_2\text{Te}_2\text{Se}$ are in very good agreement with the band structure calculations and in fact indicate that the parabolic bulk conduction band (BCB) of $\text{Sb}_2\text{Te}_2\text{Se}$ is shifted towards higher energies as compared to Sb_2Te_3 .

The electron dynamics in Sb_2Te_3 and $\text{Sb}_2\text{Te}_2\text{Se}$ at room temperature and at 40 K was compared in order to identify the main decay mechanisms of electrons in the TSS. Fig. 3(c) exemplarily shows transient data for Sb_2Te_3 employing visible (2.58 eV) pump light. The

slow rise of the transients reflects the delayed filling from higher lying states and the maximum population of the TSS is reached only up to 1 ps after the optical excitation. The decay of the 2PPE signal for larger delays can be well described by a single exponential. Two decay channels have been identified which are both related to the coupling of the TSS with bulk states. The dominating one is electron-hole pair creation in the partially filled valence band as has been also concluded for other p-doped materials [51, 52]. The decay time of electrons in the TSS therefore depends strongly on the number of unoccupied states in the valence band and it has been shown that it can be enhanced by up to two orders of magnitude by tuning the Fermi level through doping of Sb_2Te_3 with Bi [58]. In bulk insulating $\text{Bi}_2\text{Te}_2\text{Se}$, a decay time of even more than 4 μs has been observed [54]. The second important decay channel is electron transport out of the probed volume close to the surface into the bulk through coupling of the TSS to the bulk conduction band. As can be seen in Fig. 3(d), the decay time gets shorter at higher energies just where the TSS starts to degenerate with the bulk conduction band. This reduction of the decay time at higher energies is even stronger at 40 K which can be explained by the higher electron mobility in bulk Sb_2Te_3 at lower temperatures.

While these experiments mainly probed the electron transport into the bulk, the investigation of the unusual transport properties within the TSS by 2PPE requires at first the optical generation of an inhomogeneous momentum distribution in the TSS whereat an asymmetry along a certain direction corresponds to a photocurrent.

Helicity-dependent photocurrents on Bi₂Se₃

The first experiment that found a helicity-dependent photocurrent on a 3D TI was performed by McIver *et al.* [29] on Bi₂Se₃ using laser light with a photon energy of 1.56 eV [29]. The laser was focussed onto the sample in the center between two metallic contacts that picked up the induced electrical current and the helicity of the light was continuously varied by a $\lambda/4$ -plate. Beside a helicity-independent thermoelectric current due to inhomogeneous laser heating, a helicity-dependent photocurrent was found, the dependence on light helicity and angle of incidence of which just fitted the behavior expected for the circular photogalvanic effect. The photon drag effect has been ruled out because of the bulk spin degeneracy of Bi₂Se₃. Olbricht *et al.* [31], however, pointed out that a substantial photon drag effect comparable to the photogalvanic effect has even been observed in 2D materials with vanishing spin-orbit coupling such as graphene [69]. For (Bi,Sb)Te based TIs, it has been shown that the photon drag effect can even outweigh the photogalvanic effect under illumination with THz radiation at large angles of incidence [34].

Kastl *et al.* combined the pickup of the photocurrent by electrical contacts with a time-resolved detection using Au strip lines and a laser-triggered Auston-switch that allowed a time-of-flight analysis of the photogenerated hot electrons [70]. They concluded that the helicity-dependent contribution of the detected photocurrent has in fact its origin in the TSS because they found that it just travels with a group velocity that is consistent with the slope of the Dirac cone of Bi₂Se₃ at the Fermi energy.

The photon energy in these experiments exceeded the bulk band gap of the sample by far which prohibits a direct optical excitation within the Dirac cone close to E_F as has been considered by Junck *et al.* [32]. Moreover, Bi₂Se₃ is intrinsically significantly n-doped and the TSS is occupied up to energies above the conduction band minimum. This raises the question which electronic states at the surface are involved in the optical excitation and finally carry the detected photocurrent in these transport measurements. Recent experiments on gated (Bi_{1-x}Sb_x)₂Te₃ thin films, which were utilizing a similar experimental scheme as McIver *et al.*, together with first principal calculations and an analytical model suggest that the photocurrents are generated by optical transitions between the TSS and higher lying bulk bands [71].

A first more detailed insight into the electronic states that are involved in the optical excitation of Bi₂Se₃ by 1.5 eV light was provided by Niesner *et al.* [47], who demonstrated by 2PPE that the surfaces of Bi₂Te_xSe_{3-x} compounds, including Bi₂Se₃, support a second unoccupied Dirac cone at an energy of around 1.5 eV above E_F . Sobota *et al.* [50] showed shortly afterwards that

it can in fact be directly excited by 1.5-eV laser pulses in n-type Bi₂Se₃ thin films. 2PPE experiments by Ketterl *et al.* on Bi₂Se₃ bulk crystals employed circular polarized pump pulses and an electron detection in two-dimensional momentum space [61]. They have shown that 1.7-eV pump pulses provide a direct coupling between the first and second TSS, but found that the observed threefold-symmetric dichroic signal is independent of the excitation energy and only reflects the excitation pattern of the initial state. They found a small residual asymmetry, which is compatible with an unidirectional photocurrent, only in the energy region where the first TSS hybridizes with bulk states. The latter are, however, not symmetry protected and cannot carry spin-polarized photocurrents. This let them conclude that the helicity-dependent photocurrents excited by near-infrared light in Bi₂Se₃ do not reflect an intrinsic property of the TSS.

Recent 2PPE experiments on Bi₂Se₃ by Soifer *et al.* [62] showed that 3-eV pump pulses create helicity-dependent asymmetries of different sign across the unoccupied spectrum due to different resonant optical transitions, including transitions into the 2nd TSS, but that not each asymmetric distribution is associated with a TSS. All observed asymmetries decay on a time scale of the cross correlation between pump and probe pulses and no persistent asymmetry was observed.

These experiments on Bi₂Se₃ show that even if the origin of a photocurrent can be linked to the surface of a 3D TI, it is not *a priori* connected to the unusual transport properties of the TSS, which promises long-living currents with only low losses.

Helicity-dependent 2PPE on Sb₂Te₃

Motivated by the first experiments of McIver *et al.* on Bi₂Se₃ [29], we systematically explored the possibility to detect a helicity-dependent photocurrent in Sb₂Te₃ by 2PPE using pump pulses of different photon energies (0.52-1.03 , 1.55, 2.53 eV). For these, and all of experiments presented in the following, the electrons were detected in a direction perpendicular to the plane of incidence of pump and probe pulses in order to exclude the generation of a k-space asymmetry of the detected photoelectrons due to linear dichroism of the probe pulses at oblique incidence as has been observed the first experiments on Sb₂Te₃ [53]. The helicity of the initially s-polarized pump pulses was varied by rotating a $\lambda/4$ -plate which was placed in the pump beam path. Exemplarily, Fig. 4 shows the variation of the 2PPE intensity for opposite k_{\parallel} at two different energies above the Dirac point upon excitation with 2.53-eV pump pulses. The plane of light incidence was oriented along $\bar{\Gamma}-\bar{M}$ of the Sb₂Te₃ surface Brillouin zone (SBZ) and the photoelectrons were detected perpendicular to this direction along $\bar{\Gamma}-\bar{K}$. The 2PPE intensity has been normalized in Fig.4(b) and (c)

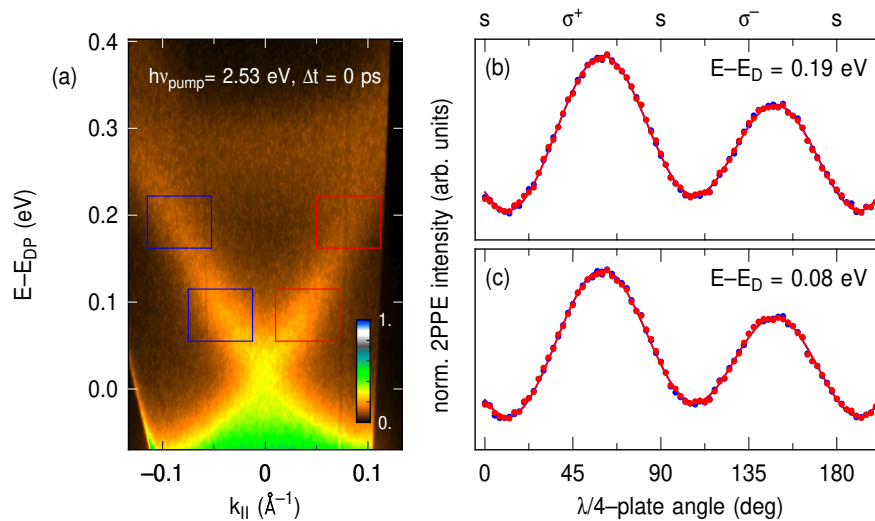


FIG. 4. (a): 2PPE spectrum of the TSS of Sb_2Te_3 at temporal overlap between UV probe and visible pump pulses. The electrons were detected along the Γ - \bar{K} direction, perpendicular to the plane of light incidence. (b) and (c): Normalized 2PPE signal at $-k_{||}$ (blue) and $+k_{||}$ (red) as a function of the polarization of the pump pulses for two energy regions as indicated by the integration windows in (a), respectively. The absence of a phase shift between the data for opposite $k_{||}$ shows that no helicity-dependent photocurrent is generated.

because a slight asymmetry is often observed because of a non perfect alignment of the sample. These plots show that the pump helicity changes the population of the TSS symmetrically but does not introduce a phase shift between opposite parallel momenta $k_{||}$. This means that the variation of the helicity simply changes the absorption of the pump pulses because of the different Fresnel coefficients for the s- and p-polarized components of the electrical field. The absence of a phase shift clearly shows that no helicity-dependent photocurrent is generated. This negative result agrees with the fact that, unlike in the case of Bi_2Se_3 , a second unoccupied TSS has not been identified for Sb_2Te_3 .

In contrast, Sanchéz-Barriga *et al.* [56], who performed spin- and time resolved photoemission experiments for Sb_2Te_3 , reported such a helicity-dependent photocurrent upon pumping with 1.5 eV and attributed it to a resonant transition from deeper-lying bulk valence-band states at ~ 1 eV below E_F to the TSS. Since the sample orientation has been used as in our experiment, this discrepancy is difficult to understand if the samples have the same electronics structure. Compared to the results of Refs. [53, 58, 72], however, the lifetime of the electrons in the TSS was found to be shorter by more than a factor of two in Ref. [56], although the position of E_F was similar.

MID-IR EXCITATION

Direct optical excitation of the TSS

In order to restrict the optical excitation to transitions in the close vicinity of the TSS, Kuroda *et al.* [72] developed a 2PPE setup that utilizes ultrashort mid-IR pump pulses with photon energies that match the bulk band gap of Sb_2Te_3 . This was realized by using a laser system that is able to pump two optical parametric amplifiers (OPA) simultaneously. A scheme of this setup together with the experimental geometry is depicted in Fig. 5. The frequency doubled output of the primarily used OPA, which is operated in the visible range, still provides the UV probe pulses. Pump pulses with photon energies of 0.2-0.4 eV were generated by difference frequency mixing of the signal and idler output of the second OPA, which is tunable in the near infrared. With these low photon energies, a novel direct optical excitation process of the TSS by a resonant transition from its occupied into its unoccupied part across the Dirac point could be revealed [72]. Moreover, it was found that even linearly polarized mid-IR light is able to produce a strong asymmetric population of the TSS in k -space. By observing the decay of the asymmetric population, the dynamics of elastic momentum scattering, which is restricted due to the protection against backscattering, could be investigated [72].

Figure 6 demonstrates the resonant optical excitation of the TSS as well as the generation of an asymmetric population in k -space for low photon energies by comparison of a 2PPE spectrum just after visible excitation

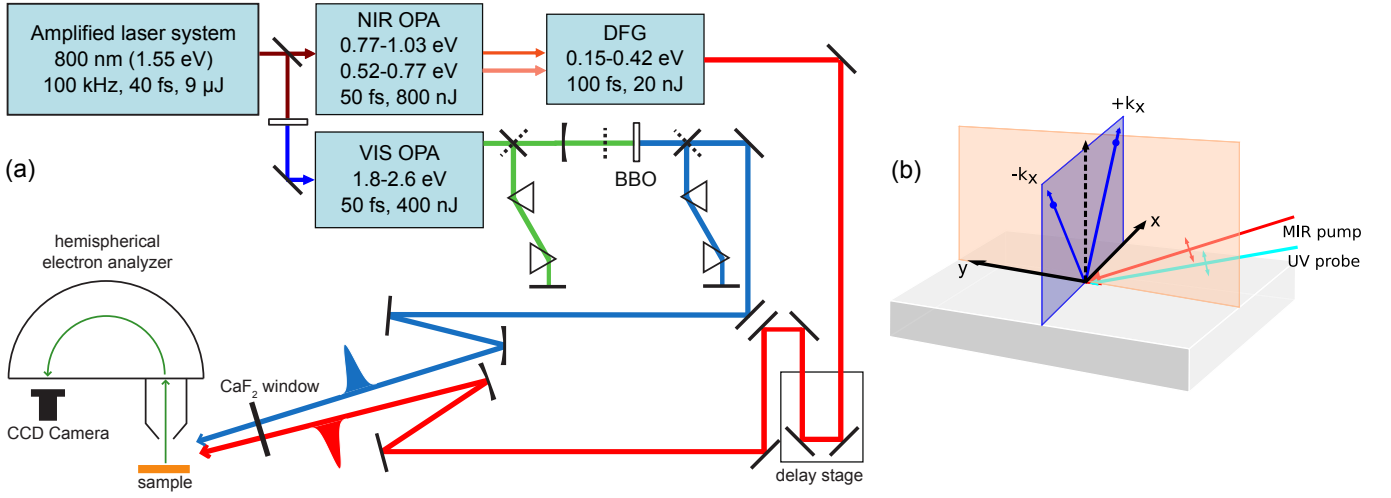


FIG. 5. (a) Experimental setup for 2PPE with mid-IR pump pulses and UV probe pulses. (b) Experimental geometry. The entrance slit of the hemispherical electron analyzer (k_x - or k_{\parallel} -direction) is oriented perpendicular to the plane of light incidence.

with spectra after excitation with mid-IR pump pulses of photon energies between 0.31 eV and 0.37 eV. It shows that only the mid-IR pump pulses generate a strongly enhanced population of the TSS at a specific energy above the Dirac point (red arrows) that shifts downwards with decreasing photon energy. By evaluating this energy position as a function of the mid-IR photon energy, it could be revealed that it originates from resonant transitions between the occupied and unoccupied part of the TSS across the Dirac point [72]. The 2PPE spectra in Fig. 6 show in addition that excitation with p-polarized mid-IR pulses also generates a strong asymmetry between the 2PPE intensity opposite k_{\parallel} . Because this asymmetry is not observed for excitation with visible pump pulses but the same UV probe pulses, linear dichroism of the photoemission probe process cannot be responsible for this asymmetry but in fact represents an asymmetric population of the TSS in k -space.

Photocurrent generation

For a one-dimensional system, a population difference for opposite k_{\parallel} can be causally equated with a macroscopic photocurrent. For the two-dimensional TSS of a tetradymite 3D TI, however, the observation of a population asymmetry along a line in the 2D k -space of the surface is a necessary but not sufficient condition for the presence of a macroscopic photocurrent because it could also result from a threefold symmetric excitation of the TSS as has been pointed out by Ketterl *et al.* [61]. In order to answer this question, we have recently employed a novel hemispherical electron analyzer (Scienta DA30) that is equipped with deflection plates in the electron lens. This makes it possible to acquire energy-momentum (E - k_x) maps with the electron momentum

k_x oriented along the orientation of the entrance slit of the hemisphere for varying momentum k_y perpendicular to k_x . In this way, the full surface band structure can be sequentially mapped in two-dimensional momentum without moving the sample. It should be noted that this method is qualitatively different from the commonly applied variation of the sample azimuth because it keeps the direction of the light incidence fixed with respect to the sample orientation. We will show in the following that the application of this technique reveals that the observed asymmetry of the population for opposite k_{\parallel} in the case of mid-IR excitation is in fact associated with a macroscopic photocurrent in the TSS.

Figure 7 compares selected cuts of the full two-dimensional surface band structure of the TSS of Sb_2Te_3 for visible and mid-IR excitation and two different sample orientations. The lower row shows E - k_x maps of the 2PPE intensity as has been presented above, whereas the middle row shows k_x - k_y maps for which the 2PPE intensity has been integrated over an energy interval that is centered at the resonantly excited energy for the mid-IR excitation.

Although the excitation with visible light results in a homogeneous population of the full Dirac cone due to sequential filling from higher-lying states, the 2PPE intensity in the k_x - k_y map shown in Fig. 7(d) reveals a reduced two-fold symmetry with a mirror axis along the direction of light incidence (k_y -direction). The data is therefore symmetric only along the k_x -direction as shown in Fig. 7(a). This asymmetry, however, does not result from an inhomogeneous population of the TSS but from the oblique incidence of the p-polarized UV probe pulses and is independent of the sample orientation as has been tested by azimuthal rotation of the sample by 90° (not shown). In general, the 2PPE intensity distribution is governed by both the transient population of the inter-

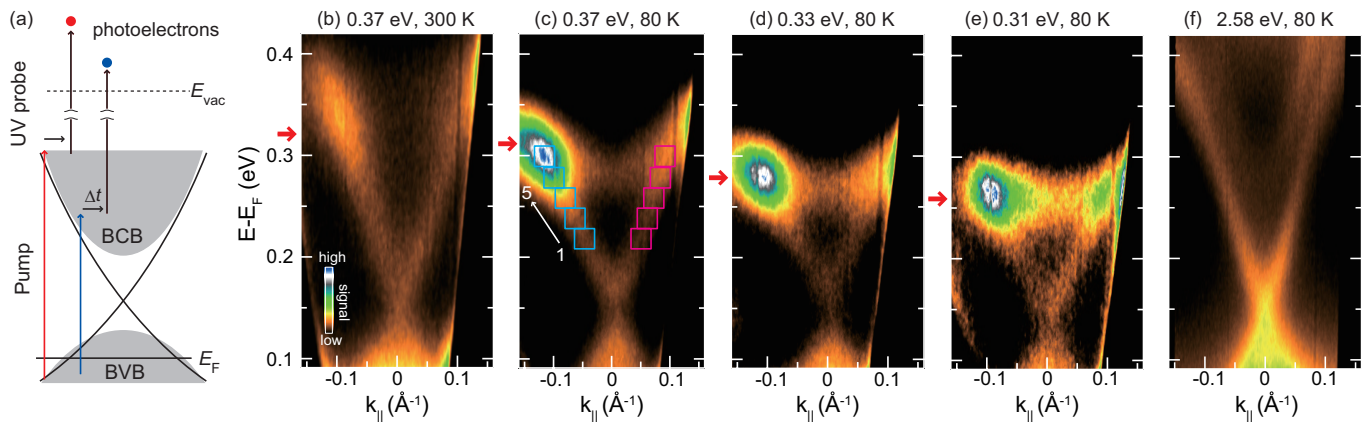


FIG. 6. (a) Excitation scheme for the population of the TSS in Sb_2Te_3 with mid-IR pump pulses and subsequent photoemission with ultraviolet probe pulses. (b) and (c) Angle-resolved 2PPE spectra for 0.37 eV pump and 5.16 eV probe pulses 50 fs after mid-IR excitation at 300 K and 80 K, respectively. The electrons were detected along a direction close to $\bar{\Gamma}\text{-}\bar{M}$, perpendicular to the plane of light incidence. Red arrows indicate the energies of maximum population enhancement in the TSS. (d) and (e) show the results acquired at 80 K using 0.35 eV and 0.31 eV pump pulses, respectively. (f) shows a spectrum for 2.58 eV pump pulses for comparison. Reproduced with permission.[72] Copyright 2016, American Physical Society.

mediate state excited by the pump pulses and the sequential photoemission by the probe pulses into the detected final states. In the case of visible excitation, any momentum dependence of the spectral weight of the 2PPE data can be related to the photoemission probe process. It depends on the polarization of the probe pulses and the symmetry of the intermediate state. For p -polarized probe pulses incident along the k_y -direction, a half moon shaped intensity distribution indicates that the TSS is dominated by out-of-plane sp_z orbitals with negligible in-plane contributions [73]. The latter would result in a threefold symmetric pattern. The k_x - k_y maps can be therefore corrected for the photoemission probe process by dividing the intensity by $(1 - \sin \phi)$ where ϕ is the azimuthal angle counting anticlockwise with respect to the $+k_x$ direction. This is, however, not applicable for ϕ close to 90° and this correction is only applied for $k_y < 0$ and mirror the data with respect to the k_x axis. The corrected and symmetrized data depicted in Fig. 7(g) shows in fact a homogeneous intensity distribution around the Dirac cone and in particular no kink at the mirror axis. Moreover, at this energy above the DP, the warping of the Dirac cone with a slight flattening of the linear dispersion along $\bar{\Gamma}\text{-}\bar{M}$ [67] becomes visible. The correction of the 2PPE intensity for the impact of the photoemission probe makes it possible to reveal the actual population in the intermediate state by this intensity correction also for other pump photon energies as long as the same photoemission probe is used. In the case of an inhomogeneous population in k -space, the mirroring of the data can, however, only be applied if a mirror axis of the sample surface is oriented perpendicular to the plane of light incidence.

A mirror axis of the three-fold symmetric surface of

$\text{Sb}_2\text{Te}_3(0001)$ is found along the $\bar{\Gamma}\text{-}\bar{M}$ direction. If this axis is oriented perpendicular the plane of incidence (k_y -direction), the 2PPE intensity reveals a strong asymmetry with respect to the k_x -direction as can be seen in Fig. 7(c). The corresponding raw and corrected k_x - k_y maps shown in Fig. 7(f) and (i), respectively, shows that the mid-IR excitation does not produce a simple two-fold symmetric population of the TSS but an enhancement of the population at three points within the Dirac cone along $\bar{\Gamma}\text{-}\bar{M}$ directions, which reflects the three-fold symmetry of the $\text{Sb}_2\text{Te}_3(0001)$ surface. Even if the photoemission probe is much less efficient in the direction of the upper right \bar{M} point, the enhancement is still faintly visible in the uncorrected data. The pattern indicates that the optical excitation is associated with the Sb-Te bonds which have a three-fold symmetric arrangement in the unit cell [74]. The degree of the population enhancement, however, differs in the three directions. Even the raw data in Fig. 7(f) clearly shows that it is much stronger in direction of the left ($\phi = 180^\circ$) as compared to that in the direction to the lower right ($\phi = -60^\circ$). Quantitatively, the corresponding 2PPE intensity is larger by 40%. This difference is further enhanced by a factor of about 1.9 when the data is corrected for the photoemission probe as shown in Fig. 7(i) but it should be emphasized that the conclusion on the asymmetric population is not based on this correction procedure. The symmetrized image shown in Fig. 7(i) should only serve for a better visualization.

These results unambiguously show that the direct excitation by the mid-IR pulses in fact generates a macroscopic photocurrent in the TSS along the k_x direction. Because of the spin texture of the TSS, this photocurrent should be automatically spin-polarized.

The magnitude and sign of the intensity asymmetry

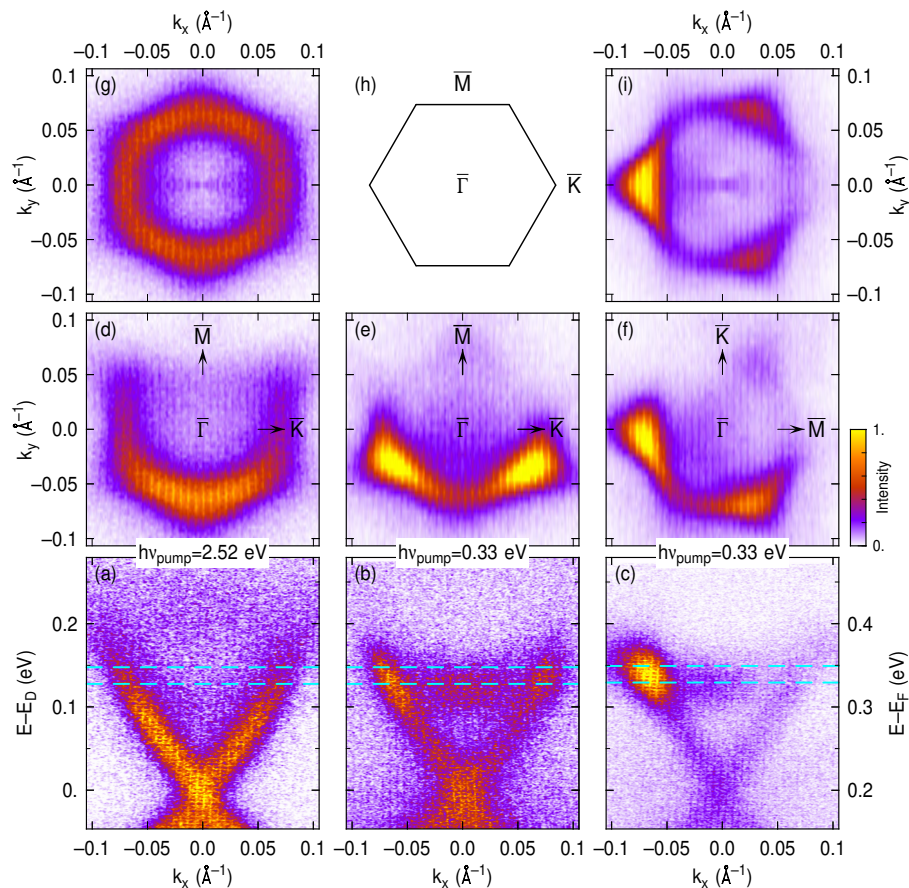


FIG. 7. Angle-resolved 2PPE data of the TSS of Sb_2Te_3 excited by visible and by mid-IR pump pulses for different sample orientations. (a) E - k_x map for 2.52-eV excitation and k_x along $\bar{\Gamma}$ - \bar{K} . (b) for 0.33-eV excitation and k_x along $\bar{\Gamma}$ - \bar{K} . (c) for 0.33-eV excitation and k_x along $\bar{\Gamma}$ - \bar{M} . (d)-(f) Corresponding k_x - k_y maps integrated over energy intervals centered at $E - E_D = 140$ meV as is depicted by the cyan dashed lines in (a)-(c). (g) and (i) show the same cuts as (d) and (f) but with the intensity corrected for the matrix element of the probe transition and symmetrized by mirroring the data at the mirror axis of the surface ($\bar{\Gamma}$ - \bar{M} -direction). For all data, the plane of light incidence is oriented along the k_y -direction. (h) Surface Brillouin zone of Sb_2Te_3 .

observed along the k_x -direction depends on the azimuthal orientation of the sample with respect to the plane of light incidence [75]. As shown in Fig. 7(b), it vanishes if the $\bar{\Gamma}$ - \bar{M} direction is oriented along the plane of incidence. In this case, the excitation pattern in the TSS has a pure three-fold symmetry and no photocurrent is generated as can be concluded from Fig. 7(e). Note that symmetrization is not possible in this three-fold symmetric distribution because the $\bar{\Gamma}$ - \bar{K} direction is not a mirror plane.

On the basis of these new results, we take the opportunity to clarify the following point. In Ref. [72], it was reported that the asymmetry for opposite k_{\parallel} was observed, if the plane of light incidence was oriented along $\bar{\Gamma}$ - \bar{M} and the electrons were detected along $\bar{\Gamma}$ - \bar{K} . For these experiments, the sample azimuth was determined by low-energy electron diffraction (LEED) with an accuracy of better than 5° with respect to the orientation of the entrance slit of the hemispherical electron analyzer.

The two-dimensional mapping of the photoelectrons presented in Fig. 7, however, makes it possible to determine the sample orientation with respect to the electron spectrometer in a direct way with the help of the warping of the Dirac cone. This reveals that the asymmetry and therewith the photocurrent is in fact generated for the opposite sample orientation. Examination of the k_x - k_y map shown in Fig. 7(e), however, makes it clear that even a small misalignment of the sample azimuth results in a strong asymmetry in the E - k_x cuts. We therefore conclude that the limited precision of the azimuth determination in Ref. [72] was responsible for the contrary assignment.

Ultrafast decay dynamics of the photocurrent

The generation of a photocurrent makes it possible to utilize 2PPE not only for the investigation of inelastic de-

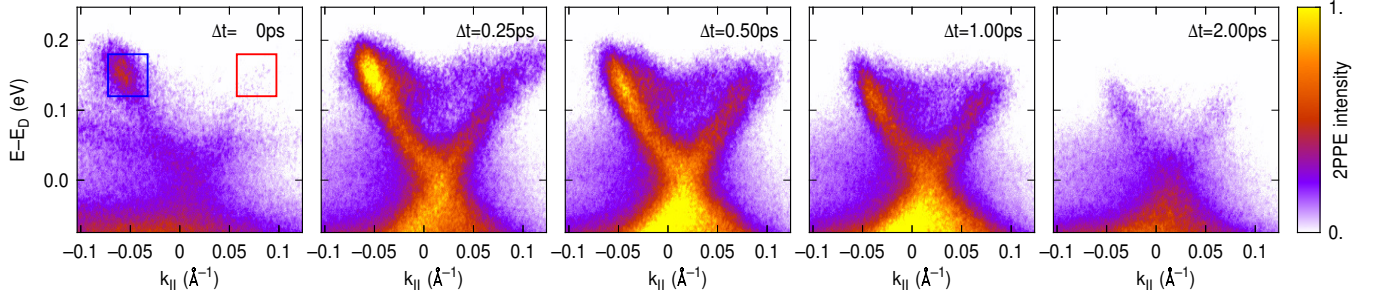


FIG. 8. Angle-resolved 2PPE spectra of Sb_2Te_3 for different delays between the mid-IR pump and the UV probe pulses. The overall time resolution (convolution of pump and probe pulses) is better than 200 fs (FWHM). The electrons were detected along a direction close to $\bar{\Gamma}-\bar{M}$, perpendicular to the plane of light incidence.

cay but makes it possible to access also elastic momentum scattering within TSS by observing the redistribution of the electron distribution in k -space as was demonstrated in Ref. [72]. In this way, it could be shown that the spin structure of the TSS in fact imposes strong restrictions on momentum scattering which are reflected by a slow homogenization of the initially inhomogeneous distribution of the electrons in momentum space. This can be already concluded from a series of 2PPE spectra for selected delays Δt between the mid-IR pump and UV probe pulses as is compiled in Fig. 8. This series shows that the population of the TSS at the resonantly excited energy has its maximum already at $\Delta t = 0.25$ ps, which reflects the direct optical excitation without delayed filling. The filling of the lower part of the Dirac cone, however, is delayed and peaks at $\Delta t = 0.5$ ps due to sequential inelastic scattering of the resonantly excited electrons to lower energies. At temporal overlap between pump and probe pulses ($\Delta t = 0$), an additional parabolic band can be observed at ~ 50 meV above the DP. This band results from population of the third image-potential state, which is in fact located close below the vacuum level but appears at a similar final state energy as the TSS. For 2PPE of image-potential states, the role of pump and probe pulses is reversed and their decay is observed for negative delays of the UV pulses with respect to the mid-IR pulses. For increasing delay, the population of the TSS gradually decreases but asymmetry between opposite k_{\parallel} is still visible even at $\Delta t = 2$ ps. This already shows that the randomization of the TSS population in k -space proceeds on a slower time scale as compared to the inelastic decay.

Figure 9 (a) shows the 2PPE intensity integrated over regions as are depicted by the blue and red rectangles shown in the most left graph of Fig. 8 at the direct excitation energy but for comparable data published in Ref. [72]. It reveals a distinct different decay dynamics for opposite k_{\parallel} . At $-k_{\parallel}$ (blue curve), the decay is initially faster and becomes slower for delays larger than ~ 750 fs. In contrast to this, the 2PPE intensity at $+k_{\parallel}$ is initially slower. For larger delays, the decay rate matches the one

observed for $-k_{\parallel}$. Both curves proceed with the same slope in the semi-logarithmic plot. The initially faster delay at $-k_{\parallel}$ and the delay response at $+k_{\parallel}$ can be explained by the transfer of the electrons from $-k_{\parallel}$ to $+k_{\parallel}$ due to momentum scattering along a circular constant energy cut of the Dirac cone. Simultaneously, the population at both k_{\parallel} decay by inelastic scattering with the same rate, which explains the common decay for larger delays.

In Ref. [72], it has been shown that the decay dynamics at opposite k_{\parallel} can be decomposed into inelastic and elastic decay with the help of a simple rate-equation model, which is depicted in the inset of Fig. 9 (a). It considers two momentum-independent effective decay rates Γ_i and Γ_e^k . Γ_i describes the decay out of the TSS that consists of true inelastic decay to lower-lying electronic states (Γ_{e-h}) as well as quasi-elastic interband scattering into the bulk conduction band (Γ_t). The latter is possible because the energy of the direct optical excitation is close to the conduction band minimum. Γ_e^k describes the rate of population exchange between opposite parallel momenta. Because 180° momentum scattering in a single event should be forbidden due to the protection of the TSS against backscattering, it represents an effective rate for in fact multiple scattering events along the two-dimensional Dirac cone. By assuming that the 2PPE intensities $I_{\pm k_{\parallel}}$ at opposite parallel momenta are proportional to the respective populations $n_{\pm k_{\parallel}}$ of the TSS, the two rate equations for $I_{+k_{\parallel}}$ and $I_{-k_{\parallel}}$ can be written as

$$\frac{dI_{\pm k_{\parallel}}}{dt} = P_{\pm k_{\parallel}} \delta(t) \pm \Gamma_e^k \Delta I - \Gamma_i I_{\pm k_{\parallel}}. \quad (1)$$

Here, $P_{\pm k_{\parallel}}$ denotes the different excitation probabilities at opposite k_{\parallel} , $\delta(t)$ the temporal profile of the Gaussian shaped mid-IR pulses, and $\Delta I = I_{-k_{\parallel}} - I_{+k_{\parallel}}$ being the intensity difference between $\pm k_{\parallel}$. Both equations can be combined into a single rate equation for ΔI

$$\frac{d\Delta I}{dt} = (P_{-k_{\parallel}} - P_{+k_{\parallel}}) \delta(t) - (2\Gamma_e^k + \Gamma_i) \Delta I, \quad (2)$$

which describes the dynamics of the photocurrent that decays exponentially with a time constant $\tau_c =$

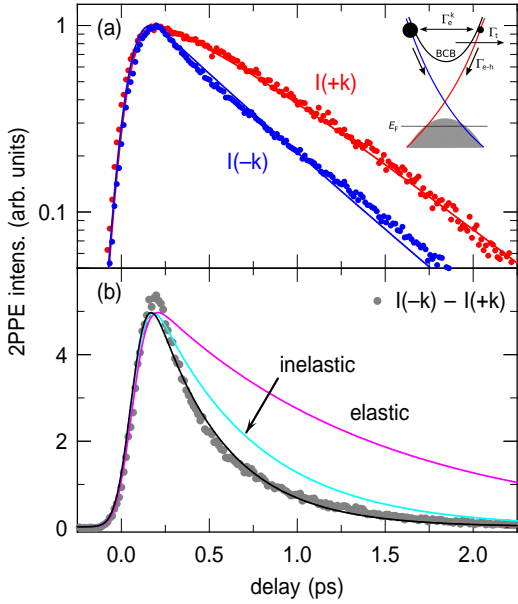


FIG. 9. (a) Normalized 2PPE intensity of the transient population in the Dirac cone of Sb_2Te_3 at opposite parallel momenta k_{\parallel} (data points). Solid lines are fits to the data (see text). The two data sets have been obtained by integration of the 2PPE intensity over blue and red rectangles such as shown in Fig. 8 but for data published in Ref. [72]. The inset shows a scheme of the rate-equation model for fitting the data. (b) Intensity difference $\Delta I = I_{-k_{\parallel}} - I_{+k_{\parallel}}$ (grey dots). The black line shows a fit that considers elastic momentum scattering and inelastic decay. The magenta and cyan lines show these contributions separately. Reproduced with permission.[75] Copyright 2017, Society of Photo-Optical Instrumentation Engineers (SPIE)

$1/(2\Gamma_e^k + \Gamma_i)$. The best fits of the data, which are shown by the solid lines in Fig. 9, yield $\tau_c = 0.42$ ps, $\tau_i = 1/\Gamma_i = 0.6$ ps and $\tau_e = 1/\Gamma_e^k = 2.5$ ps.

The characteristic time for elastic momentum scattering τ_e is therefore considerably longer as compared to the inelastic decay time τ_i . It is also much longer if compared, e.g. with electrons in surface states of well-prepared noble metal surfaces [18, 76, 77]. By considering that the electrons in the TSS move with a Fermi velocity of $v_F = 3 \text{ \AA}/\text{fs}$, which corresponds to the slope of the Dirac cone of the TSS, an elastic scattering time of $\tau_e = 2.5$ ps corresponds to a mean free path of $\lambda_e = v_F \tau_e = 0.75 \mu\text{m}$. This is almost two orders of magnitude larger as compared to the typical mean distance between defects of less than 100 \AA on such cleaved surface as has been reported by scanning tunneling microscopy (STM) [66] and represents a manifestation of the suppression of backscattering scattering within the TSS.

Polarization control of the photocurrent

Although the spin texture of the TSS suggests that a photocurrent, i.e. an asymmetry of the population for opposite k_{\parallel} , should be controllable by optical excitation of different helicity [27], the experiments presented in sections - have shown that a strong photocurrent can be already generated by linear polarized mid-IR pulses if the $\bar{\Gamma}-\bar{K}$ direction of the sample is oriented along the plane of light incidence. In Ref. [78], it has been shown that a variation of the light helicity by introducing a rotatable $\lambda/4$ -waveplate in the pump beam results only in a small change of the observed asymmetry of the intensity for opposite k_{\parallel} of less than 10%.

Here, we show by novel data that the magnitude as well as the sign of the asymmetry can be controlled by the pump helicity if the $\bar{\Gamma}-\bar{M}$ direction of the sample is oriented along the plane of light incidence. For this sample orientation, no photocurrent is generated by p-polarized mid-IR pulses and no asymmetry is observed along the $\bar{\Gamma}-\bar{K}$ direction as shown in Figs. 7(b) and (e). Figure 10 demonstrates the polarization control of the photocurrent in Sb_2Te_3 in this case with Fig. 10(a)-(c) showing angle-resolved 2PPE spectra for three selected orientations α of a $\lambda/4$ -waveplate that was introduced in the mid-IR pump beam. The orientation $\alpha = 90^\circ$ used for Figure 10(b) corresponds to p-polarized mid-IR pulses and results in an almost vanishing intensity difference for opposite k_{\parallel} . The small residual asymmetry can be attributed to a not perfect orientation of the sample azimuth. Figure 10(a) and (c) show that the magnitude of the asymmetry can be enhanced as well as its sign can be switched by changing of the waveplate angle by -60° and $+60^\circ$, respectively. The control of the asymmetry is most pronounced at the resonantly excited energy as shown in Figs. 10(d) and (e) which show difference plots of Figs. 10(a) and (c) with respect to Fig. 10(b). These two figures show that rotation of the $\lambda/4$ -waveplate by -60° ($+60^\circ$) enhances the intensity at $+k_{\parallel}$ ($-k_{\parallel}$) and simultaneously reduces it at the opposite parallel momentum. These two orientations of the $\lambda/4$ -waveplate induce the most strongest change of the asymmetry as can be seen in Fig. 10(g) where the intensity difference for opposite k_{\parallel} at the resonantly excited energy is plotted as a function of α . Following the analysis of McIver *et al.* [29], it can be decomposed into contributions of the circular and linear photogalvanic effect by fitting the asymmetry as follows,

$$I_{-k_{\parallel}}(\alpha) - I_{+k_{\parallel}}(\alpha) = C \sin 2\alpha + L_1 \sin 4\alpha + L_2 \cos 4\alpha + D. \quad (3)$$

Here, C describes the helicity-dependent circular photogalvanic effect. The coefficient L_1 has been attributed to helicity-independent linear photogalvanic effect and L_2 to a modulation of the absorptivity [29, 70]. The parameter D considers a polarization-independent back-

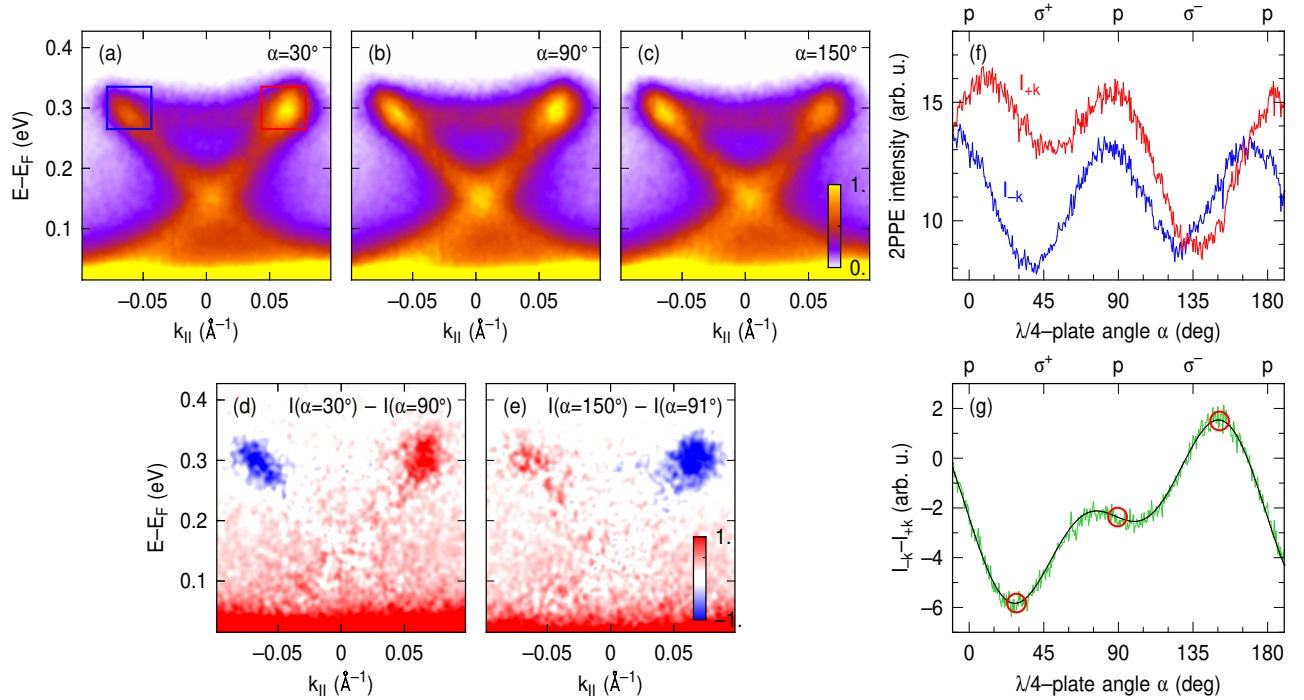


FIG. 10. Helicity control of the photocurrent. (a)-(c) Angle-resolved 2PPE spectra of Sb₂Te₃ for three different orientations of a $\lambda/4$ -waveplate in the mid-IR pump beam. The $\bar{\Gamma}$ - \bar{M} direction of the sample was oriented along the plane of light incidence. Electrons were collected along $\bar{\Gamma}$ - \bar{K} . (d) Intensity difference between spectra (b) and (a). (e) Difference between (c) and (b). (f) 2PPE intensity for opposite $k_{||}$ as a function of $\lambda/4$ -waveplate angle integrated over the blue and red square depicted in (a). (g) Difference ($I_{-k_{||}} - I_{+k_{||}}$) of the intensities plotted in (f). The solid black line show a fit through the data. The three red circles mark the rotation angles used for (a)-(c), respectively.

ground that results here from the non-perfect azimuthal alignment of the sample. The fit shown in Fig. 10(g) yields $C = -2.56(2)$, $L_1 = -1.68(2)$, $L_2 = -0.16(2)$, and $D = -2.92(1)$. It should be noted that the data can be equally well fitted by omitting L_2 but allowing instead a small misalignment of the $\lambda/4$ -waveplate from the nominal orientation $\alpha' = \alpha + \alpha_0$ with $\alpha_0 = 0.5(1)^\circ$. The contribution of the circular photogalvanic effect to the photocurrent is in both cases for these data almost twice as large as compared to the linear photogalvanic effect. Due to the contribution of the linear photogalvanic effect, the maximum asymmetry is not reached for left- and right-circular pump light ($\alpha = 45^\circ$ and $\alpha = 135^\circ$, respectively) but still symmetrically with respect to $\alpha = 90^\circ$ for elliptical polarized light at $\alpha = 60^\circ$ and $\alpha = 150^\circ$, respectively.

In summary, these results demonstrate that full optical control of the photocurrent by the light helicity is possible for this particular sample orientation but the magnitude of the helicity-dependent asymmetry is small. This is in line with the observations of Ketterl *et al.* [61], who found for the same sample orientation also only a small helicity-dependent asymmetry for excitation of Bi₂Se₃ with 1.7-eV pulses. As shown in section , a much larger photocurrent can be generated along the $\bar{\Gamma}$ - \bar{M} direction

by using linear-polarized mid-IR pulses incident along the $\bar{\Gamma}$ - \bar{K} direction.

THZ-DRIVEN TSS CURRENTS

The mid-IR excitation scheme makes it possible to generate persistent photocurrents in the TSS by an optical interband excitation. Its combination with time- and angle-resolved 2PPE allows for a very detailed investigation of the scattering processes of optically excited electrons in the initially unoccupied TSS of Sb₂Te₃ and could verify their large ballistic mean free path. In a real device application, however, the electron transport will be induced by electric fields through intraband acceleration and proceeds close to the Fermi level. Therefore, the most direct way to investigate electron transport on a microscopic level is to observe how an electric field accelerates electrons close to E_F .

Recently, such an experiment has been realized by a combination of THz excitation with time-resolved ARPES [79]. This approach makes it possible to observe directly on a subcycle time scale how the carrier wave of a terahertz light pulse accelerates Dirac fermions in the TSS. While terahertz streaking of photo-emitted electrons in the vacuum traces the electromagnetic field

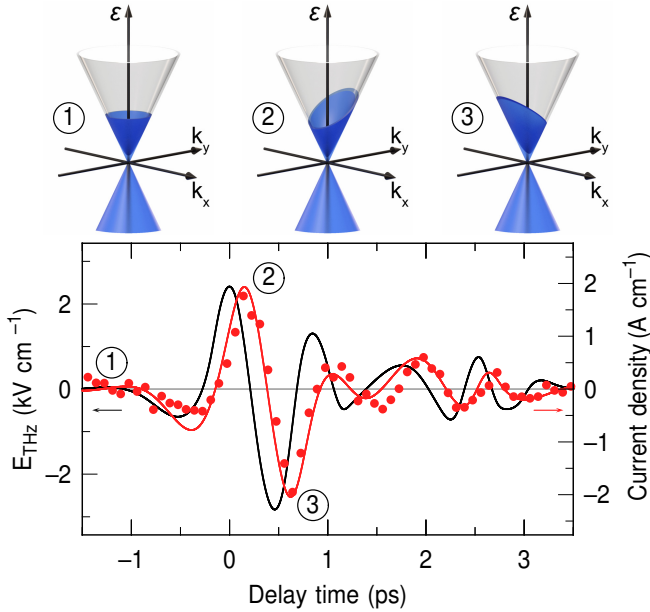


FIG. 11. Temporal evolution of the current density in the TSS of Bi_2Te_3 induced by a strong THz electric field pulse with a center frequency of 1 THz (data points). The red solid curve shows a simulation of the current dynamics using an elastic momentum scattering time of 1 ps and an electric field transient that has been determined *in situ* and that is plotted as black solid line (see Ref. [79] for details). The sketches illustrate the acceleration of the Dirac fermions back and forth in the topological surface for three selected delays before the arrival of the THz transient (1), at the time of maximum acceleration in $+k_y$ -direction (2), and at the time of maximum acceleration in the opposite direction (3). Adapted with permission.[79] Copyright 2018, Springer Nature.

at the surface, the acceleration of the electron in the TSS leads to a strong redistribution of electrons in momentum space. This has been demonstrated for Bi_2Te_3 where the Fermi level is located well above the Dirac point but below the conduction band minimum at the $\bar{\Gamma}$ -point.

In contrast to the mid-IR excitation, no persistent photocurrent is generated in this experiment because the net acceleration integrated over the complete transient of the electric field vanishes. The subcycle observation of the redistribution of the Fermi-Dirac distribution, however, makes it possible to investigate the interplay of back and forth acceleration by the electric field transient and the scattering of the electrons in the TSS just around the Fermi level.

Figure 11 summarizes the main results of this work. The sketches illustrate the back and forth acceleration of the electrons in the TSS of Bi_2Te_3 which occupy the TSS up to energies of 200 meV above E_F . The black solid line depicts the time-evolution of the s-polarized electric field with a center frequency of 1 THz. It has been determined *in situ* from the momentum streaking of the electrons in front of the surface. Because of the conti-

nuity of the s-polarized electric field component across the interface between vacuum and the sample, this just corresponds to the field that accelerates the electrons in the TSS along the surface. The data points show the transient current density that has been calculated from asymmetry of the photoelectron spectra at opposite k_{\parallel} and the electron density in the TSS. The time lag of the current density with respect to the electric field already demonstrates that the electrons sample energy and momentum during the acceleration without much losses on the time scale of the period of the THz transient. The inertia-free surface currents are protected by spin-momentum locking and reach peak densities as large as 2 A/cm. They travel with the Fermi velocity of 4.1 Å/fs or 410 nm/ps. Comparison of the measured current with the results of a semiclassical Boltzmann model depicted as red solid line shows that the relevant scattering times of the electrons carrying the current amount to at least 1 ps. This is a comparable to the results on Sb_2Te_3 and demonstrates that 3D topological insulators have in fact the potential to build ultrafast low-loss electronic devices driven by light waves.

CONCLUSIONS AND OUTLOOK

The work presented here shows that time- and angle-resolved 2PPE is a versatile tool to selectively observe the optical generation of photocurrents and their decay in the TSS of 3D TIs. It allows to disentangle the decay of the photocurrent by elastic and inelastic electron scattering and to verify the exceptional transport properties in the TSS due to its particular spin texture. This applies in particular for the excitation with ultrashort low-energy light pulses in the mid-IR range, which have shown to permit a direct optical excitation of the TSS of Sb_2Te_3 across the Dirac point. Surprisingly, even linear polarized mid-IR excitation is able to generate a strong photocurrent in the TSS while the helicity-dependence of the excitation is found to be small. For certain sample orientations, however, the latter provides a full optical control of the magnitude and sign of the photocurrent. The mapping of the surface band structure in two dimensions has shown to be important for the distinction between population asymmetries along one direction that simply result from a threefold symmetric excitation and those which are representative for an actual macroscopic photocurrent. 2D-mapping of electron redistribution within the full Dirac cone opens the possibility to access the ultrafast dynamics of optically as well as THz induced photocurrents in unprecedented detail. It makes it possible to observe momentum scattering of arbitrary scattering angle and to investigate the effect of the warping of the Dirac cone on the electron and photocurrent dynamics. It will furthermore enable to study how defects introduced by nonmagnetic or magnetic dopants affect

not only the band structure of the TSS but also inelastic and elastic momentum scattering. This is of great interest because doping of 3D TIs by nonmagnetic elements is typically used for tuning the Fermi level while doping with magnetic elements is one route to realize the quantum anomalous Hall effect [80].

Acknowledgements

We thank R. Reimann, K. Kuroda, E. V. Chulkov, K. A. Kokh, O. E. Tereshchenko, A. Kimura, S. Schlauderer, C. P. Schmid, F. Langer, S. Baierl, C. Lange, and R. Huber for a fruitful and pleasant collaboration in this work. We gratefully acknowledge funding by the Deutsche Forschungsgemeinschaft (DFG, German Research Foundation) through grant numbers HO 2295/7 (SPP 1666), GU 495/2 and project ID 223848855-SFB 1083.

-
- [1] L. Fu, C. L. Kane, E. J. Mele, *Phys. Rev. Lett.* **2007**, *98*, 10.
- [2] Y. Xia, D. Qian, D. Hsieh, L. Wray, A. Pal, H. Lin, A. Bansil, D. Grauer, Y. S. Hor, R. J. Cava, M. Z. Hasan, *Nat. Phys.* **2009**, *5* 398.
- [3] H. J. Zhang, C. X. Liu, X. L. Qi, X. Dai, Z. Fang, S. C. Zhang, *Nat. Phys.* **2009**, *5* 438.
- [4] M. Z. Hasan, C. L. Kane, *Rev. Mod. Phys.* **2010**, *82* 3045.
- [5] D. Hsieh, Y. Xia, D. Qian, L. Wray, J. H. Dil, F. Meier, J. Osterwalder, L. Patthey, J. G. Checkelsky, N. P. Ong, A. V. Fedorov, H. Lin, A. Bansil, D. Grauer, Y. S. Hor, R. J. Cava, M. Z. Hasan, *Nature* **2009**, *460* 1101.
- [6] J. González, F. Guinea, M. Vozmediano, *Phys. Rev. Lett.* **1996**, *77*, 17 3589.
- [7] P. Roushan, J. Seo, C. V. Parker, Y. S. Hor, D. Hsieh, D. Qian, A. Richardella, M. Z. Hasan, R. J. Cava, A. Yazdani, *Nature* **2009**, *460*, 7259 1106.
- [8] L. Fu, C. L. Kane, *Phys. Rev. B* **2007**, *76*, 4.
- [9] J. Navrátil, J. Horák, T. Plecháček, S. Kamba, P. Lošťák, J. Dyck, W. Chen, C. Uher, *J. Solid State Chem.* **2004**, *177*, 4-5 1704.
- [10] Y. S. Hor, A. Richardella, P. Roushan, Y. Xia, J. G. Checkelsky, A. Yazdani, M. Z. Hasan, N. P. Ong, R. J. Cava, *Phys. Rev. B* **2009**, *79* 195208.
- [11] Y. L. Chen, J. G. Analytis, J. H. Chu, Z. K. Liu, S. K. Mo, X. L. Qi, H. J. Zhang, D. H. Lu, X. Dai, Z. Fang, S. C. Zhang, I. R. Fisher, Z. Hussain, Z. X. Shen, *Science* **2009**, *325* 178.
- [12] D. Hsieh, D. Qian, L. Wray, Y. Xia, Y. S. Hor, R. J. Cava, M. Z. Hasan, *Nature* **2008**, *452*, 7190 970.
- [13] E. Dupont, P. B. Corkum, H. C. Liu, M. Buchanan, Z. R. Wasilewski, *Phys. Rev. Lett.* **1995**, *74* 3596.
- [14] R. Atanasov, A. Haché, J. L. P. Hughes, H. M. van Driel, J. E. Sipe, *Phys. Rev. Lett.* **1996**, *76* 1703.
- [15] A. Haché, Y. Kostoulas, R. Atanasov, J. L. P. Hughes, J. E. Sipe, H. M. van Driel, *Phys. Rev. Lett.* **1997**, *78* 306.
- [16] M. J. Stevens, A. L. Smirl, R. D. R. Bhat, A. Najmaie, J. E. Sipe, H. M. van Driel, *Phys. Rev. Lett.* **2003**, *90* 136603.
- [17] J. Hübner, W. W. Rühle, M. Klude, D. Hommel, R. D. R. Bhat, J. E. Sipe, H. M. van Driel, *Phys. Rev. Lett.* **2003**, *90* 216601.
- [18] J. Gütde, M. Rohleder, T. Meier, S. W. Koch, U. Höfer, *Science* **2007**, *318* 1287.
- [19] D. A. Bas, K. Vargas-Velez, S. Babakiray, T. A. Johnson, P. Borisov, T. D. Stanescu, D. Lederman, A. D. Bristow, *Appl. Phys. Lett.* **2015**, *106* 041109.
- [20] D. A. Bas, R. A. Muniz, S. Babakiray, D. Lederman, J. E. Sipe, A. D. Bristow, *Opt. Express* **2016**, *24* 23583.
- [21] C. Aversa, J. E. Sipe, *Phys. Rev. B* **1995**, *52* 14636.
- [22] R. A. Muniz, J. E. Sipe, *Phys. Rev. B* **2014**, *89*, 20.
- [23] S. D. Ganichev, W. Prettl, *J. Phys.-Condens. Mat.* **2003**, *15* R935.
- [24] I. L. Ivchenko, *Optical spectroscopy of semiconductor nanostructures*, Alpha Science Int'l Ltd., Harrow, **2005**.
- [25] S. D. Ganichev, W. Prettl, *Intense Terahertz Excitation of Semiconductors*, Oxford University Press, Oxford, **2006**.
- [26] Y. B. Zhang, T. T. Tang, C. Girit, Z. Hao, M. C. Martin, A. Zettl, M. F. Crommie, Y. R. Shen, F. Wang, *Nature* **2009**, *459* 820.
- [27] P. Hosur, *Phys. Rev. B* **2011**, *83* 035309.
- [28] Y. Q. Huang, I. A. Buyanova, W. M. Chen, *Sci. Rep.* **2020**, *10*, 1.
- [29] J. W. McIver, D. Hsieh, H. Steinberg, P. Jarillo-Herrero, N. Gedik, *Nat. Nanotechnol.* **2012**, *7* 96.
- [30] J. Duan, N. Tang, X. He, Y. Yan, S. Zhang, X. Qin, X. Wang, X. Yang, F. Xu, Y. Chen, W. Ge, B. Shen, *Sci. Rep.* **2014**, *4*.
- [31] P. Olbrich, L. E. Golub, T. Herrmann, S. N. Danilov, H. Plank, V. V. Bel'kov, G. Mussler, C. Weyrich, C. M. Schneider, J. Kampmeier, D. Grützmacher, L. Plucinski, M. Eschbach, S. D. Ganichev, *Phys. Rev. Lett.* **2014**, *113* 096601.
- [32] A. Junck, G. Refael, F. von Oppen, *Phys. Rev. B* **2013**, *88* 075144.
- [33] A. A. Grinberg, *Sov. Phys. JETP* **1970**, *31*, 3 531.
- [34] H. Plank, L. E. Golub, S. Bauer, V. V. Bel'kov, T. Herrmann, P. Olbrich, M. Eschbach, L. Plucinski, C. M. Schneider, J. Kampmeier, M. Lanius, G. Mussler, D. Grützmacher, S. D. Ganichev, *Phys. Rev. B* **2016**, *93*, 12.
- [35] R. Haight, *Surf. Sci. Rep.* **1995**, *21* 277.
- [36] T. Fauster, W. Steinmann, In P. Halevi, editor, *Electromagnetic Waves: Recent Developments in Research*, volume 2, 347–411. North-Holland, Amsterdam, **1995**.
- [37] U. Bovensiepen, H. Petek, M. Wolf, editors, *Dynamics at Solid State Surfaces and Interfaces*, Vol. 1: *Current Developments*, Wiley-VCH, Berlin, **2010**.
- [38] W. Berthold, U. Höfer, P. Feulner, E. V. Chulkov, V. M. Silkin, P. M. Echenique, *Phys. Rev. Lett.* **2002**, *88* 056805.
- [39] M. Rohleder, K. Duncker, W. Berthold, J. Gütde, U. Höfer, *New J. Phys.* **2005**, *7* 103.
- [40] H. Petek, S. Ogawa, *Prog. Surf. Sci.* **1997**, *56* 239.
- [41] J. Gütde, M. Rohleder, U. Höfer, *Appl. Phys. A* **2006**, *85* 345.
- [42] M. Reutzler, A. Li, Z. Wang, H. Petek, *Nat. Commun.* **2020**, *11* 2230.
- [43] Y. H. Wang, D. Hsieh, E. J. Sie, H. Steinberg, D. R. Gardner, Y. S. Lee, P. Jarillo-Herrero, N. Gedik, *Phys. Rev. Lett.* **2012**, *109* 127401.
- [44] A. Crepaldi, B. Ressel, F. Cilento, M. Zacchigna,

- C. Grazioli, H. Berger, P. Bugnon, K. Kern, M. Grioni, F. Parmigiani, *Phys. Rev. B* **2012**, *86* 205133.
- [45] M. Hajlaoui, E. Papalazarou, J. Mauchain, G. Lantz, N. Moisan, D. Boschetto, Z. Jiang, I. Miotkowski, Y. P. Chen, A. Taleb-Ibrahimi, L. Perfetti, M. Marsi, *Nano Lett.* **2012**, *12* 3532.
- [46] J. A. Sobota, S. Yang, J. G. Analytis, Y. L. Chen, I. R. Fisher, P. S. Kirchmann, Z. X. Shen, *Phys. Rev. Lett.* **2012**, *108* 117403.
- [47] D. Niesner, T. Fauster, J. I. Dadap, N. Zaki, K. R. Knox, P. C. Yeh, R. Bhandari, R. M. Osgood, M. Petrovic, M. Kralj, *Phys. Rev. B* **2012**, *85* 081402.
- [48] A. Crepaldi, F. Cilento, B. Ressel, C. Cacho, J. C. Johanssen, M. Zacchigna, H. Berger, P. Bugnon, C. Grazioli, I. C. E. Turcu, E. Springate, K. Kern, M. Grioni, F. Parmigiani, *Phys. Rev. B* **2013**, *88* 121404.
- [49] M. Hajlaoui, E. Papalazarou, J. Mauchain, Z. Jiang, I. Miotkowski, Y. P. Chen, A. Taleb-Ibrahimi, L. Perfetti, M. Marsi, *Eur. Phys. J.-Spec. Top.* **2013**, *222* 1271.
- [50] J. A. Sobota, S. L. Yang, A. F. Kemper, J. J. Lee, F. T. Schmitt, W. Li, R. G. Moore, J. G. Analytis, I. R. Fisher, P. S. Kirchmann, T. P. Devereaux, Z. X. Shen, *Phys. Rev. Lett.* **2013**, *111* 136802.
- [51] D. Niesner, S. Otto, V. Hermann, T. Fauster, T. V. Menshchikova, S. V. Eremeev, Z. S. Aliev, I. R. Amiraslanov, M. B. Babanly, P. M. Echenique, E. V. Chulkov, *Phys. Rev. B* **2014**, *89* 081404. Erratum *Phys. Rev. B* **2015**, *91* 039903.
- [52] M. Hajlaoui, E. Papalazarou, J. Mauchain, L. Perfetti, A. Taleb-Ibrahimi, F. Navarin, M. Monteverde, P. Auban-Senzier, C. R. Pasquier, N. Moisan, D. Boschetto, M. Neupane, M. Z. Hasan, T. Durakiewicz, Z. Jiang, Y. Xu, I. Miotkowski, Y. P. Chen, S. Jia, H. W. Ji, R. J. Cava, M. Marsi, *Nat. Commun.* **2014**, *5* 3003.
- [53] J. Reimann, J. Gdde, K. Kuroda, E. V. Chulkov, U. Hfer, *Phys. Rev. B* **2014**, *90* 081106. Erratum: *Phys. Rev. B* **2015**, *91* 039903.
- [54] M. Neupane, S. Y. Xu, Y. Ishida, S. Jia, B. M. Fregoso, C. Liu, I. Belopolski, G. Bian, N. Alidoust, T. Durakiewicz, V. Galitski, S. Shin, R. J. Cava, M. Z. Hasan, *Phys. Rev. Lett.* **2015**, *115* 116801.
- [55] S. Zhu, Y. Ishida, K. Kuroda, K. Sumida, M. Ye, J. Wang, H. Pan, M. Taniguchi, S. Qiao, S. Shin, A. Kimura, *Sci. Rep.* **2015**, *5* 13213.
- [56] J. Snchez-Barriga, E. Golias, A. Varykhalov, J. Braun, L. V. Yashina, R. Schumann, J. Minar, H. Ebert, O. Kornilov, O. Rader, *Phys. Rev. B* **2016**, *93* 155426.
- [57] C. Jozwiak, J. A. Sobota, K. Gotlieb, A. F. Kemper, C. R. Rotundu, R. J. Birgeneau, Z. Hussain, D.-H. Lee, Z.-X. Shen, A. Lanzara, *Nature Commun.* **2016**, *7*.
- [58] K. Sumida, Y. Ishida, S. Zhu, M. Ye, A. Pertsova, C. Triola, K. A. Kokh, O. E. Tereshchenko, A. V. Balatsky, S. Shin, A. Kimura, *Sci. Rep.* **2017**, *7*, 1 14080.
- [59] D. Bugini, F. Boschini, H. Hedayat, H. Yi, C. Chen, X. Zhou, C. Manzoni, C. Dallera, G. Cerullo, E. Carpene, *J. Phys. Condens. Matter* **2017**, *29*, 30.
- [60] J. Snchez-Barriga, M. Battiato, M. Krivenkov, E. Golias, A. Varykhalov, A. Romualdi, L. V. Yashina, J. Minr, O. Kornilov, H. Ebert, K. Held, J. Braun, *Phys. Rev. B* **2017**, *95* 125405.
- [61] A. S. Ketterl, S. Otto, M. Bastian, B. Andres, C. Gahl, J. Minar, H. Ebert, J. Braun, O. E. Tereshchenko, K. A. Kokh, T. Fauster, M. Weinelt, *Phys. Rev. B* **2018**, *98* 155406.
- [62] H. Soifer, A. Gauthier, A. F. Kemper, C. R. Rotundu, S.-L. Yang, H. Xiong, D. Lu, M. Hashimoto, P. S. Kirchmann, J. A. Sobota, Z.-X. Shen, *Phys. Rev. Lett.* **2019**, *122* 167401.
- [63] J. Hork, Z. Stary, J. Klikorka, *phys. stat. sol. (b)* **1988**, *147* 501.
- [64] C. Pauly, G. Bihlmayer, M. Liebmann, M. Grob, A. Georgi, D. Subramaniam, M. R. Scholz, J. Snchez-Barriga, A. Varykhalov, S. Blugel, O. Rader, M. Morgenstern, *Phys. Rev. B* **2012**, *86* 235106.
- [65] C. Seibel, H. Maass, M. Ohtak, S. Fiedler, C. Junger, C. H. Min, H. Bentmann, K. Sakamoto, F. Reinert, *Phys. Rev. B* **2012**, *86* 161105.
- [66] Y. Jiang, Y. Wang, M. Chen, Z. Li, C. Song, K. He, L. Wang, X. Chen, X. Ma, Q.-K. Xue, *Phys. Rev. Lett.* **2012**, *108* 016401.
- [67] T. V. Menshchikova, S. V. Eremeev, E. V. Chulkov, *JETP Lett.* **2011**, *94* 106.
- [68] H. Lin, T. Das, L. A. Wray, S. Y. Xu, M. Z. Hasan, A. Bansil, *New J. Phys.* **2011**, *13* 095005.
- [69] M. M. Glazov, S. D. Ganichev, *Phys. Rep.* **2014**, *535* 101.
- [70] C. Kastl, C. Krnetzky, H. Karl, A. W. Holleitner, *Nat. Commun.* **2015**, *6* 6617.
- [71] Y. Pan, Q.-Z. Wang, A. L. Yeats, T. Pillsbury, T. C. Flanagan, A. Richardella, H. Zhang, D. D. Awschalom, C.-X. Liu, N. Samarth, *Nature Commun.* **2017**, *8*.
- [72] K. Kuroda, J. Reimann, J. Gdde, U. Hfer, *Phys. Rev. Lett.* **2016**, *116* 076801.
- [73] S. Moser, *J. Electron Spectrosc.* **2017**, *214* 29.
- [74] Y. D. Glinka, S. Babakiray, T. A. Johnson, M. B. Holcomb, D. Lederman, *Phys. Rev. B* **2015**, *91* 195307.
- [75] K. Kuroda, J. Reimann, J. Gdde, U. Hfer, *Proc. SPIE 10102, Ultrafast Phenomena and Nanophotonics XXI* **2017** 101020 71.
- [76] T. Fauster, M. Weinelt, U. Hfer, *Prog. Surf. Sci.* **2007**, *82* 224.
- [77] M. Marks, C. H. Schwalb, K. Schubert, J. Gdde, U. Hfer, *Phys. Rev. B* **2011**, *84* 245402.
- [78] K. Kuroda, J. Reimann, K. A. Kokh, O. E. Tereshchenko, A. Kimura, J. Gdde, U. Hfer, *Phys. Rev. B* **2017**, *95* 081103(R).
- [79] J. Reimann, S. Schlauderer, C. P. Schmid, F. Langer, S. Baierl, K. A. Kokh, O. E. Tereshchenko, A. Kimura, C. Lange, Gdde, U. Hfer, R. Huber, *Nature* **2018**, *562* 396.
- [80] Y. Tokura, K. Yasuda, A. Tsukazaki, *Nat. Rev. Phys.* **2019**, *1* 126.